Aerodynamic Interaction Between an Over-the-Wing Propeller and the Wing Boundary-Layer in Adverse Pressure Gradients

de Vries, Reynard; van Arnhem, Nando; Avallone, Francesco; Ragni, Daniele; Vos, Roelof; Eitelberg, Georg; Veldhuis, Leo

DOI
10.2514/6.2019-3035

Publication date
2019

Document Version
Final published version

Published in
AIAA Aviation 2019 Forum

AIAA AVIATION Forum
17-21 June 2019, Dallas, Texas
AIAA Aviation 2019 Forum

10.2514/6.2019-3035

Aerodynamic Interaction Between an Over-the-Wing Propeller and the Wing Boundary-Layer in Adverse Pressure Gradients

Reynard de Vries*, Nando van Arnhem†, Francesco Avallone‡, Daniele Ragni§, Roelof Vos¶, Georg Eitelberg‖ and Leo L. M. Veldhuis**
Delft University of Technology, Kluyverweg 1, 2629HS Delft, The Netherlands

This experimental study focuses on the aerodynamic interaction effects that occur between an over-the-wing (OTW) propeller and a wing boundary-layer. An OTW propeller is positioned above the hinge-line of a wing featuring a plain flap. The measurements are carried out with and without axial pressure gradients by deflecting the flap and by extending the wing in streamwise direction to simulate a flat-plate configuration, respectively. Wing pressure taps and phase-free particle-image-velocimetry (PIV) are used to quantify the time-averaged interaction effects, while embedded microphones and phase-locked PIV are used to analyze unsteady interaction effects. Results show that the propeller generates an adverse pressure gradient on the wing surface which increases linearly with thrust and decreases as the blade tip-clearance is increased. The pressure gradient is partially caused by the slipstream contraction, which creates a streamwise velocity deficit near the wall immediately behind the propeller disk. Moreover, the rotation of the propeller blades generates pressure fluctuations on the surface, the amplitude of which exceeds both the pressure fluctuations produced by the tip-vortices and the time-averaged pressure effect of the slipstream. Consequently, the propeller triggers flow separation when the flap is deflected. A parametric study of different propeller locations indicates that increasing the tip-clearance is not an effective way to mitigate flow separation. However, displacing the propeller half a radius upstream induces a Coanda effect which allows the flow to remain attached.

I. Introduction

In order to meet the expected growth in air traffic while limiting the environmental impact of the aviation industry, novel aircraft configurations with improved propulsion-system integration are required [1, 2]. Throughout the last decade, numerous studies have identified hybrid-electric propulsion (HEP) as an enabling technology to achieve this goal [3–5]. An important benefit of HEP is the flexibility it offers in terms of power distribution, which enables more efficiently integrated propulsion systems [6, 7]. Over-the-wing (OTW) propellers present a synergistic benefit when combined with HEP, since they increase the lift-to-drag ratio of the wing [8, 9] and reduce flyover noise [10, 11], while allowing low-wing configurations with short landing-gear struts. Nevertheless, several drawbacks have limited the use of OTW propellers. These include a reduced propulsive efficiency when compared to tractor propellers [8, 12], increased thrust-induced pitching moment, and the need of large support pylons. However, the scalability of electrical motors allows the propulsive power to be divided over multiple adjacent OTW propellers without compromising the motor's specific weight or efficiency, thus reducing the diameter of each propulsor while maintaining an equivalent disk loading. This layout, known as over-the-wing distributed propulsion (DP) [13], can partially mitigate the penalties associated with large OTW propellers [14].

Earlier studies show that it is possible to estimate the aero-propulsive performance of OTW propellers in cruise conditions using panel methods [14] or RANS simulations [15]. However, predicting the high-lift performance of these systems is a difficult challenge. The work of Müller et al. [16] has shown that steady RANS simulations are insufficient to accurately predict the aerodynamic interaction between an OTW propeller and the wing when the flap is deflected. The authors identified the unsteady interaction between the propeller tip-vortices and the wing boundary-layer as a

*PhD Candidate, Flight Performance and Propulsion Section, Faculty of Aerospace Engineering, R.deVries@tudelft.nl, AIAA Member.
†PhD Candidate, Flight Performance and Propulsion Section, Faculty of Aerospace Engineering, AIAA Member.
‡Assistant Professor, Aeroacoustics Section, Faculty of Aerospace Engineering, AIAA Member.
§Assistant Professor, Aeroacoustics Section, Faculty of Aerospace Engineering, AIAA Member.
¶Assistant Professor, Flight Performance and Propulsion Section, Faculty of Aerospace Engineering, AIAA Associate Fellow.
‖Full Professor, Flight Performance and Propulsion Section, Faculty of Aerospace Engineering, AIAA Member.
**Full Professor, Flight Performance and Propulsion Section, Faculty of Aerospace Engineering, AIAA Member.

possible cause of flow separation over the flap, which was not captured in steady analyses. Both theoretical [17] and experimental [18] studies have shown that vortex–boundary-layer interaction can indeed lead to local flow separation [19]. It is also known that, during a parallel blade–vortex encounter, a convecting vortex produces pressure fluctuations on the wall surface and increases the turbulent energy in the boundary layer [20]. However, these studies do not consider the presence of a rotor close to the wall. The experiments of Murray et al. [21] show that, in that case, flow reversal can occur locally beneath the rotor and that additional unsteady vortical structures are formed, comparable to the ground-vortex effect encountered on propeller aircraft at low advance ratios [22]. Similar phenomena were observed in propeller-hull interaction studies [23, 24]. However, these studies were performed with a flat wall, and therefore provide no information regarding the impact of blade–boundary-layer interaction on flow separation when an additional pressure gradient is generated by the flap. This constitutes a large challenge for the design process of OTW distributed-propulsion systems, since these interaction effects have a significant impact on the maximum lift coefficient of the wing, but cannot be predicted without high-fidelity simulations or complex experiments.

The objective of this paper is therefore to study the steady and unsteady aerodynamic interaction effects that occur between an OTW propeller and the wing boundary-layer. Due to the difficulty of modeling this unsteady, three-dimensional, viscous problem numerically without validation data, an experimental approach is considered necessary as a first step. Measurements are performed with a plain flap and in a flat-plate configuration, in order to identify how the interaction with the boundary layer is affected by an external pressure gradient. Furthermore, different thrust settings, boundary-layer thicknesses, and propeller tip-clearances are analyzed in order to establish the impact of each of these parameters on the aerodynamic interaction phenomena. A single propeller is used in this study in order to isolate these phenomena from the additional ones which would appear if multiple adjacent propulsors were considered. The wing and propeller models are described in Sec. II along with the employed measurement techniques. Section III then discusses the aerodynamic characteristics of the propeller and isolated wing, in order to establish the conditions under which the aerodynamic interaction effects are studied. A detailed description of these effects is then provided in Sec. IV and Sec. V, which present the time-averaged and unsteady components of the phenomena, respectively. Finally, in Sec. VI a parametric study is performed in order to identify possible design strategies which mitigate flow separation.

II. Experimental Setup

A. Wind Tunnel Facility and Models

The experiments were performed in the closed-circuit, low-speed, low-turbulence tunnel (LTT) at Delft University of Technology. This tunnel presents a maximum freestream velocity of 120 m/s and inflow turbulence levels below 0.07% for the freestream velocities considered in this study ($U_\infty \leq 40$ m/s). The closed test-section has a cross-section of 1.8 m $\times$ 1.25 m. A straight, untapered wing was placed vertically in the test section as depicted in Fig. 1, at an angle-of-attack of zero degrees. The propeller was positioned in close proximity to the suction-side surface of the wing by means of a horizontal support sting, as shown in Fig. 1. The support sting could either be mounted on a balance (see Sec. II.B.1), or on a three-axes traversing system, both located outside the test section.

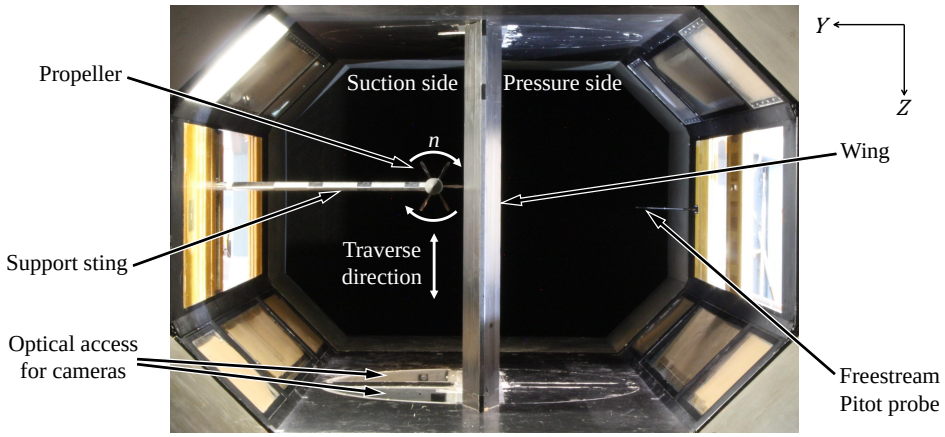

Fig. 1 Rear view of the test section indicating the position of the wing and propeller, as well as the direction of rotation and the traverse directions of the propeller.

1. Wing Geometry and Operating Conditions

The wing profile was designed with the objective of obtaining a simple curvature at the flap which could be removed in order to test the interaction effects without pressure gradients on the wing surface. The resulting profile, shown in Fig. 2a, presents a chord* of $c = 1.02$ m, and a thickness-to-chord ratio of 11%. The leading-edge geometry follows a modified super-ellipse of aspect ratio 6 up to 32% chord, in order to provide a continuous curvature [25]. Both the suction and pressure sides are then extended parallel to the wing chord-line up to 80% chord, which corresponds to the axial position of the flap hinge. The flap hinge is located near the pressure side, generating a tangent circular arc with a radius of curvature equal to 10% chord on the suction side of the flap, which is approximately equal to the propeller radius. Behind the arc, the flap surface extends the remaining 20% of the chord to the trailing edge. The upper and lower surfaces of the flap can be split and aligned in axial direction in order to elongate the flat surface of the wing. In this way, by placing an additional body of the same thickness as the wing in the test section (see Fig. 2b), the pressure gradient surrounding the flap region is minimized. Two wind-tunnel campaigns were performed, the first of which focused only on the flat-plate configuration. Between the two campaigns, minor corrections were made to the leading edge geometry, since preliminary results showed that the wing surface geometry near the leading edge differed from the specifications due to difficulties during the manufacturing process of the wing skin. The resulting changes in pressure distribution were verified to have a negligible impact on the interaction effects discussed in this study.

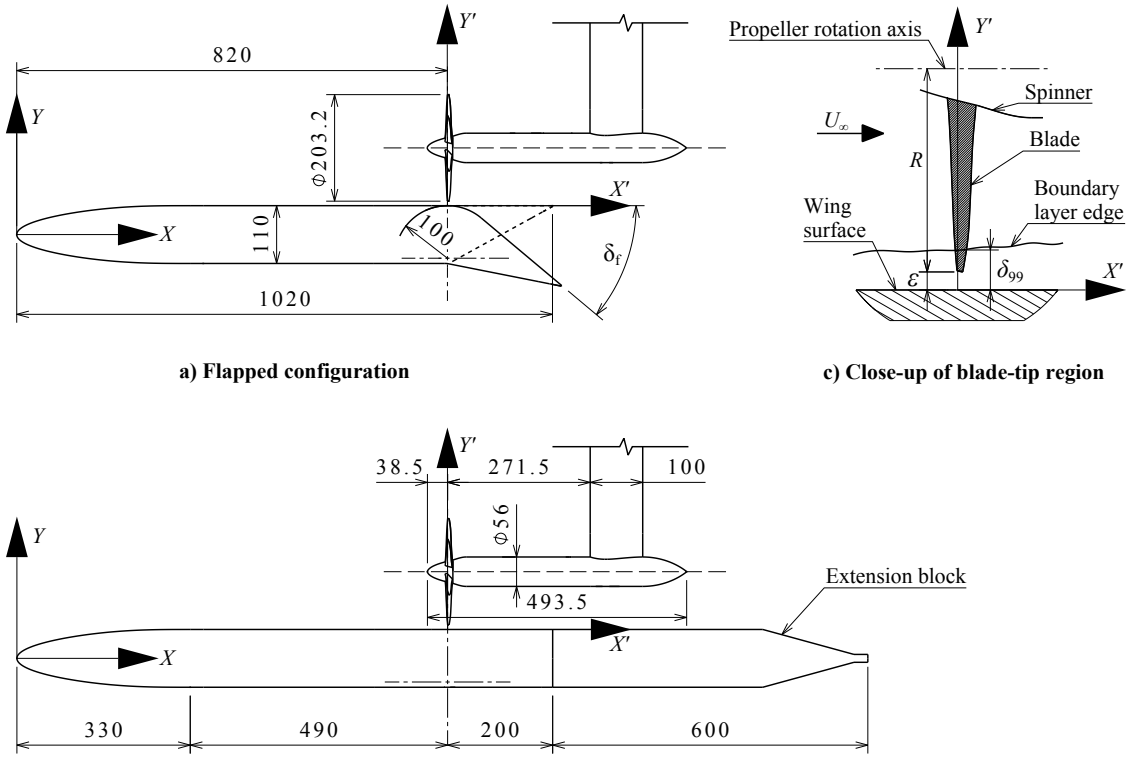

Fig. 2 Side views and main dimensions of the propeller and wing profile in a) flapped configuration and b) flat-plate configuration, including c) a close-up of the blade tip region. All dimensions expressed in mm.

Measurements were carried out at $U_\infty = 40 \pm 0.05$ m/s in order to maximize the Reynolds number ($Re_c = 2.76 \cdot 10^6$) without exceeding the maximum input level of the microphones or the maximum power of the electrical motor that drove the propeller, as well as at $U_\infty = 20 \pm 0.05$ m/s ($Re_c = 1.38 \cdot 10^6$), in order to increase the maximum thrust coefficient. Two boundary-layer configurations were analyzed. The first, named "BL1", corresponded to the turbulent boundary-layer obtained with a 3 mm wide trip-strip of distributed roughness elements with an average diameter of 530 μm (carborundum particles of grit size 36) located at 7.5% chord on both sides of the wing. The second, "BL2", was a

*The reference chord-length is taken as the length of the profile when the flap is retracted ($\delta_f = 0^o$). Since the upper surface of the flap presents a fowler motion when deflected, the true chord varies.

thicker turbulent boundary-layer obtained by increasing the equivalent surface roughness. This was done by extending the patch of carborundum particles from 7.5% chord to 32% chord on the suction side. After analyzing multiple flap deflection angles, an angle of $\delta_f = 20^o$ was selected to study the interaction phenomena in more detail, since for this deflection angle, the flow remained attached over the flap hinge but started to separate towards the trailing edge.

2. Propeller Geometry and Operating Conditions

For the majority of the measurements, the propeller was positioned above the flap hinge ($X_p/c = 0.8$), which was identified as an axial location with a good compromise between lift gain, drag reduction, and propulsive-efficiency loss in previous work [14]. A six-bladed steel propeller was used, with a diameter of $D_p = 2R = 0.2032$ m ($D_p/c = 0.2$) and blade pitch of $45^o \pm 0.05^o$ at 70% of the blade radius. The propeller is a 1:2 scale model of the one used by Li et al. [26], with a modified trailing edge to ensure a minimum thickness during the manufacturing process. The propeller was operated at advance ratios between $J = 1.0$ and $J = 2.0$ at $U_\infty = 20$ m/s, and between $J = 1.7$ and $J = 2.3$ at $U_\infty = 40$ m/s. The rotational speed of the propeller was controlled with an accuracy of ± 0.1 Hz which, together with the velocity uncertainty, corresponds to fluctuations in advance ratio below $\pm 0.5\%$. Furthermore, the clearance between the propeller blade tips and the wing surface, ε (see Fig. 2c), was varied in order to analyze the impact of tip clearance on the interaction effects. The tip-clearances were selected as (sub-)multiples of the boundary layer thickness, as defined in Sec. II.B.2. Finally, a subset of measurements were taken with the propeller at $X_p/c = 0.75$, in order to determine the influence of the propeller's axial position on flow separation.

B. Measurement Techniques

The following subsections provide an overview of the measurement techniques used during the experiment. The measured velocities and pressures were corrected for wind-tunnel blockage caused by the wing, following the image method described in Ref. [27]. Lift interference corrections were not applied, since only low lift coefficients were attained ($C_L \approx 0.1$). Propeller slipstream and support sting blockage corrections were neglected, since their combined effect was estimated to be below 0.9%.

1. External Balance

The propeller was installed on an external six-component balance to measure propeller thrust. The balance presented an uncertainty of ± 0.02 N in the range of forces measured in the experiment. The installation was designed such that the propeller axis was located at the mid-span of the wing when connected to the balance. The measurements were averaged over 30 seconds for each data point. Several points were repeated to verify the reproducibility of the measurements. In order to obtain the net forces generated by the propeller blades and spinner, all measurements were carried out both with the propeller on (indicated with the subscript "on"), and with the propeller removed and replaced by a dummy spinner (indicated with the subscript "off"). The net thrust, T, is then defined as $T = T_{on} - T_{off}$. It should be noted that the thrust force therefore includes the change in drag on the nacelle and support sting due to the propeller slipstream. In this study, two definitions of the thrust coefficient are used. The first, $C_T = T/(\rho_\infty n^2 D_p^4)$, is used to present the propeller performance curves, while the second, $T_c = T/(0.5\rho_\infty U_\infty^2 A_p)$, is used when discussing the impact of the propeller on the wing. Note that $C_T = \pi T_c J^2/8$, where $J = U_\infty/(nD_p)$ is the advance ratio of the propeller, and that ρ_∞, n, and $A_p = \pi D_p^2/4$ refer to the freestream density, rotational speed of the propeller, and propeller disk area, respectively.

The uncertainty of the thrust measurements was calculated taking into account uncertainties in the blade pitch angle, propeller alignment, and balance readings, as well as the data spread of repeated measurements due to, for example, variations in operating conditions. For this, the sensitivity of propeller thrust to blade pitch angle ($\partial C_T/\partial \beta$) and angle-of-attack ($\partial C_T/\partial \alpha_p$) were obtained from experimental and numerical data of the isolated propeller [28]. The uncertainties are included as error-bars in the results of Sec. III.B.

2. Total Pressure Probe

A pressure probe was traversed in negative Y-direction at $X/c = 0.8$ in order to characterize the total pressure distribution in the flow over the isolated wing (i.e., with the propeller installation removed) at the axial position of the propeller disk. There were two reasons for this. Firstly, the total pressure p_t was measured in the boundary layer in order to determine the boundary-layer thickness. Secondly, the pressure profiles were sampled at different spanwise locations in order to confirm that the low aspect ratio and surface imperfections of the wing did not significantly alter the two-dimensionality of the flow. The measurement sweep started at 0.5 mm ($0.005R$) clearance from the wing surface, and was traversed up to 240.5 mm ($2.37R$) clearance. The pressure was measured at 57 locations for each of the three spanwise positions

sampled ($Z/R = 0, -0.9$, and $+0.9$), with a higher resolution in the vicinity of the wing surface. Pressure data were averaged over 30 seconds for each point.

In this paper, the total pressure coefficient is defined as $C_{p,\mathrm{t}} = (p_\mathrm{t} - p_{\mathrm{t}_\infty})/q_\infty + 1$, where $q_\infty = 0.5\rho_\infty U_\infty^2$ is the freestream dynamic pressure and p_{t_∞} is the total pressure of the freestream, measured by an additional Pitot probe installed in the test section upstream of the model (see Fig. 1). The boundary layer thickness, δ_{99}, was determined as the distance from the surface where the total pressure reached 0.99^2 times the total pressure of the freestream, that is, where $C_{p,\mathrm{t}} = 0.98$. The resulting pressure profiles are presented in Sec. III.A along with error-bars which include the measurement uncertainty of the total pressure sensors (±4 Pa) and the spread in the data due to spanwise variations in the boundary-layer profile.

3. Wing Surface Pressure Taps

The wing was instrumented with 81 static pressure taps in order to evaluate the time-average impact of the propeller on the wing pressure distribution. These taps were distributed with a higher density near the leading edge and near the flap hinge. They followed a zig-zag pattern along the wing skin in order to reduce possible disturbances created by each hole on the downstream one. The holes were located at $Z = \pm 15$ mm, i.e., 15 mm above or below the mid-span location of the wing. Due to the geometrical constraints surrounding the flap mechanism, no zig-zag pattern was followed in this region, as visible in Fig. 3. Data points were averaged over 30 seconds acquisition time per measurement. A subset of measurements were repeated at the start and the end of the experiment to verify the reproducibility of results. The spread in the data of the repeated measurements, along with the uncertainty of the measurement sensors of static pressure ports (±1 Pa), are indicated by the error-bars included in Sec. IV.

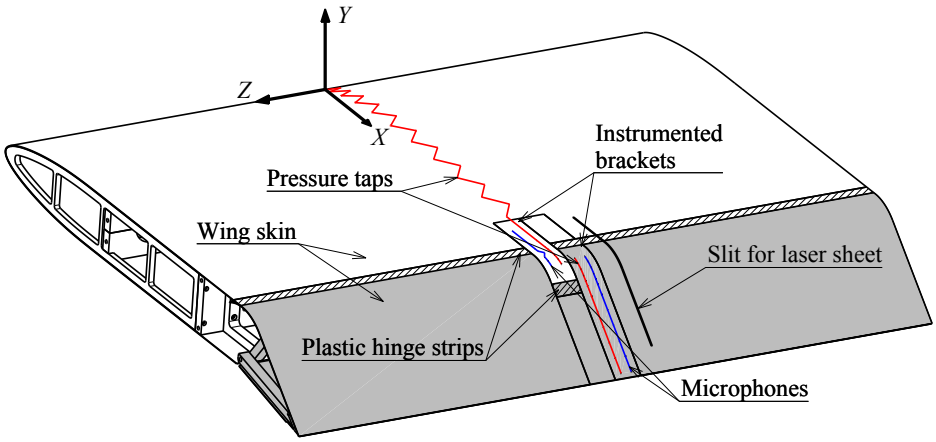

Fig. 3 Axonometric view of the suction side of the wing model, indicating the location of pressure taps (red) and embedded microphones (blue). The elements that constitute the flap are shaded in gray.

Two types of static pressure measurements were taken. In the first, the propeller was installed on an external traversing system and moved in Z-direction, mapping the pressure response on the wing surface below the propeller. For these measurements, the propeller was traversed 150 mm in each direction ($z/R = \pm 1.5$), sampling at 51 spanwise locations in total. In the second type of measurement, the propeller—connected to the balance—was positioned at the mid-span location of the wing, and the pressure distribution was recorded along the line of pressure taps. In this case, the resulting pressure distribution did not correspond exactly to the mid-section of the wing, due to the zig-zag pattern. The difference was quantified by analyzing the spanwise pressure distribution obtained during the Z-sweeps, and included as uncertainty in the results.

4. Wing Surface Microphones

The wing was instrumented with nineteen Sonion 8044 microphones, in order to map the unsteady pressure response on the wing surface below the propeller slipstream. Twelve microphones were installed on the instrumented bracket on the flap (at $Z = 35$ mm), and seven on the instrumented bracket upstream of the flap (at $Z = -35$ mm), as indicated in Fig. 3. The microphones measured in a frequency range of 10 Hz–15 kHz, with a maximum input level of 123.5 dB (re $20 \cdot 10^{-6}$ Pa) at 1 kHz and an equivalent noise level of 35 dBA. A frequency-dependent calibration was carried out using a LinearX M53 reference microphone, which was in turn calibrated by means of a GRAS 42AA piston phone.

Microphone data were acquired synchronously with the propeller encoder's once-per-revolution trigger signal using an array of National Instruments 9234 DAQ modules. The microphone data were recorded in tandem with the wing pressure data during the Z-sweeps of the propeller. At each point, the signals were measured at a sampling frequency of 51.2 kHz during 30 seconds, which corresponds to approximately 1,500 to 3,500 propeller revolutions (i.e., 9,000 to 21,000 blade passages), depending on the rotational speed of the propeller. Although no quantitative uncertainty analysis was carried out, a comparison of repeated measurements showed that the amplitude of the tonal components differed by less then 1 dB. Furthermore, the levels recorded during the measurements were verified to be at least 25 dB, typically 45 dB, above the background noise levels recorded with the wind tunnel off.

5. Particle Image Velocimetry

A stereoscopic particle image velocimetry (PIV) setup was used to obtain qualitative and quantitative information of the velocity field in the propeller slipstream and wing boundary layer. Two fields-of-view were considered. The main, large field-of-view (FOV) was set up downstream of the propeller between the nacelle and the wing surface, as shown in Fig. 4. A second, high-resolution FOV focused on the region surrounding the blade tips. A SAFEX Twin Fog DP generator with SAFEX Inside Nebelfluid was used for flow seeding. The mixture of diethylene-glycol and water generates tracer particles with an average diameter and relaxation time of the order of 1 µm and 1 µs, respectively. A 200 mJ Quantel Evergreen laser was used for illumination, positioned outside the test section on the pressure side of the wing. The light was directed through the wing with a dedicated slit in the wing and flap skin (see Figs. 3 and 4), generating a laser sheet of 2 mm thickness. Both slits were covered with a transparent plastic sheet of 0.2 mm thickness to prevent the through-flow of air. Two LaVision Imager sCMOS cameras were placed below the test section, focusing on the FOV through two transparent floor plates shown in Fig. 1. These 16-bit cameras feature a 2560 x 2160 pixel sensor with a pixel size of 6.5 µm, and were employed with Nikkor 105 mm $f/8$ and Nikkor 200 mm $f/8$ lenses for the large and small FOVs, respectively. The images were were recorded at 15 Hz and processed using LaVision Davis 8.4 software. For installed propeller measurements, 600 uncorrelated images were acquired, in addition to 300 phase-locked images at selected phase angles and 300 images with the propeller blades removed (i.e., wing and nacelle only). The main characteristics of the PIV setup are gathered in Table 1.

Table 1 Main parameters of the PIV setup.

FOV	Large	Small
Focal length [mm]	105	200
Field of view [mm^2]	100×150	50×65
Pulse delay [µs] (U_∞ = 20 m/s)	25	10
Imaging resolution [pixel/mm]	19	41
Window size [pixel^2]	24	24
Overlap factor [%]	50	50
Vector spacing [mm]	0.6	0.3
Velocity uncertainty [%]	2.5	2.75

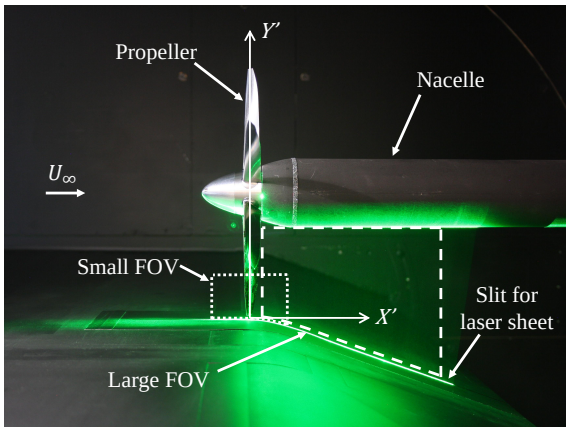

Fig. 4 Side view of the FOVs analyzed.

III. Aerodynamic Characterization of the Setup

This section describes the aerodynamic characteristics of the isolated wing and the propeller, to establish the conditions under which the interaction effects are studied in subsequent sections. To this end, Sec. III.A presents the pressure distribution and boundary-layer profiles on the wing, while Sec. III.B presents the propeller performance curves.

A. Isolated Wing Characteristics

Figure 5 shows the pressure-coefficient distributions obtained on the wing surface, with the propeller and support sting removed. In the flat-plate configuration, the difference between the pressure and suction sides of the wing is negligible, and the pressure gradient is small for $X/c > 0.4$. However, several imperfections are visible. Firstly, small pressure peaks are generated around $X/c = 0.82$, due to steps in the surface geometry at the overlap from the main element to the flap. Secondly, towards the trailing edge, the difference between the pressure side and suction side increases,

indicating that the flap surfaces—which were aligned with the downstream extension block (see Fig. 2)—were not parallel. Nevertheless, these variations are small when compared to the influence of the propeller. Furthermore, for both the flat-plate and the flapped configuration, a pressure peak is generated around $X/c = 0.08$ by the trip strip, while additional suction is generated around $X/c = 0.22$ due to a flaw in the curvature of the wing skin. However, these peaks occur far upstream of the region of interest ($\Delta X \approx 6R$), and are therefore irrelevant to the interaction phenomena.

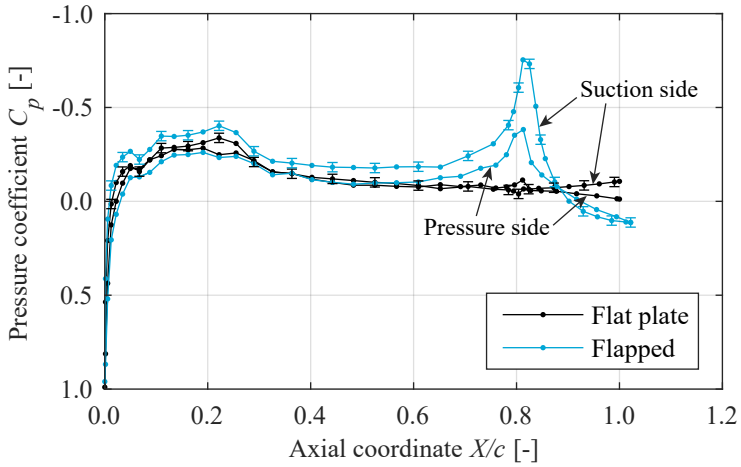

Fig. 5 Isolated-wing pressure distributions in the flat plate and flapped configuration (U_∞ = 20 m/s). Error-bars are only presented on the suction side for clarity.

When the flap is deflected, an appreciable pressure peak is generated over the flap, as shown in Fig. 5. The pressure distribution on the suction side tends towards a horizontal plateau near $X/c = 1$, indicating that the flow has separated at the trailing edge. This was confirmed during the experiment by placing tufts. For the given flap deflection of $\delta_f = 20^o$, a suction peak is also generated on the pressure side, since the surface is convex near the flap hinge. Together, this leads to a low sectional lift coefficient of $c_l = 0.1$.

The boundary-layer profiles of the isolated wing were also measured, in order to determine the boundary-layer thickness, δ_{99}. The resulting total-pressure profiles are presented for two freestream velocities in Fig. 6. Figure 6a presents the two profiles sampled for the flat-plate configuration. When the boundary layer is tripped (BL1), the boundary-layer thickness is $\delta_{99}/R = 0.14$, while with an increase in surface roughness (BL2), the thickness increases to $\delta_{99}/R = 0.20$. This 43% increase in boundary-layer thickness corresponds to an increase in the equivalent turbulent

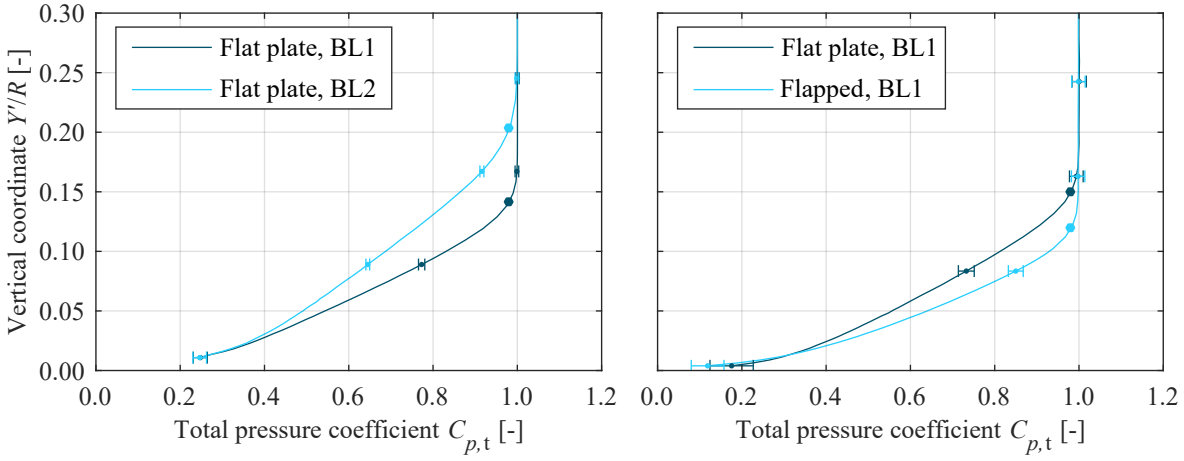

a) U_∞= 40 m/s **b) U_∞= 20 m/s**

Fig. 6 Boundary-layer profiles on the wing surface at X/c = 0.8, with the propeller and support sting removed. Round markers indicate the vertical coordinate corresponding to δ_{99}.

flat-plate Reynolds number[†] from $Re_{FP} = 1.8 \cdot 10^6$ to $Re_{FP} = 2.8 \cdot 10^6$, and thus the two boundary-layers are considered distinct enough to represent the effect of Reynolds number on the interaction with the boundary layer. In Fig. 6b, on the other hand, both profiles correspond to a boundary-layer trip (BL1). The flat-plate boundary-layer is thicker than in Fig. 6a due to the lower freestream velocity. It is also thicker than the profile obtained with the flap deflected, since for the latter the increased velocity over the wing increases the equivalent Reynolds number. The values of δ_{99} are summarized in Table 2. The different propeller tip-clearances are selected as multiples of these values. Note that, when the flap is deflected, the propeller tip-clearance is still selected as a multiple of the flat-plate boundary-layer thickness. In this way, the same absolute separation between the blade tips and the wing surface (ε/R) is kept, and thus the time-average pressure effect of the propeller on the wing is maintained.

Table 2 Boundary-layer thicknesses (δ_{99}/R), and propeller tip-clearance values (ε/R) and nomenclature.

U_∞ = 40 m/s			U_∞ = 20 m/s		
Configuration	δ_{99}/R	ε/R	**Configuration**	δ_{99}/R	ε/R
Flat plate (BL1)	0.14	0.07 (05BL1)	Flat plate (BL1)	0.15	0.037 (025BL1)
		0.14 (10BL1)			0.075 (05BL1)
		0.28 (20BL1)			
Flat plate (BL2)	0.20	0.10 (05BL2)	Flapped, $\delta_f = 20^o$	0.12	0.037 (025BL1)
		0.20 (10BL2)			0.15 (10BL1)
		0.40 (20BL2)			0.44 (30BL1)

B. Propeller Performance

The propeller performance is described here to quantify the impact of the wing and its boundary layer on propeller thrust, since this in turn affects the impact of the propeller on the wing. To this end, Fig. 7 presents the thrust coefficient of the installed propeller versus advance ratio for the different measurement cases. Performance data of the isolated propeller can be found in Ref. [28]. To improve readability, error-bars are only shown for the thrust curves which presented the largest spread in repeated measurements. Figure 7a shows that, in the flat plate configuration, the thickness of the boundary layer and the tip-clearance of the propeller have no appreciable effect on propeller thrust. Therefore, the ingestion of the boundary layer has a negligible impact on propeller performance for the boundary-layer thicknesses considered ($\delta_{99}/R < 0.2$).

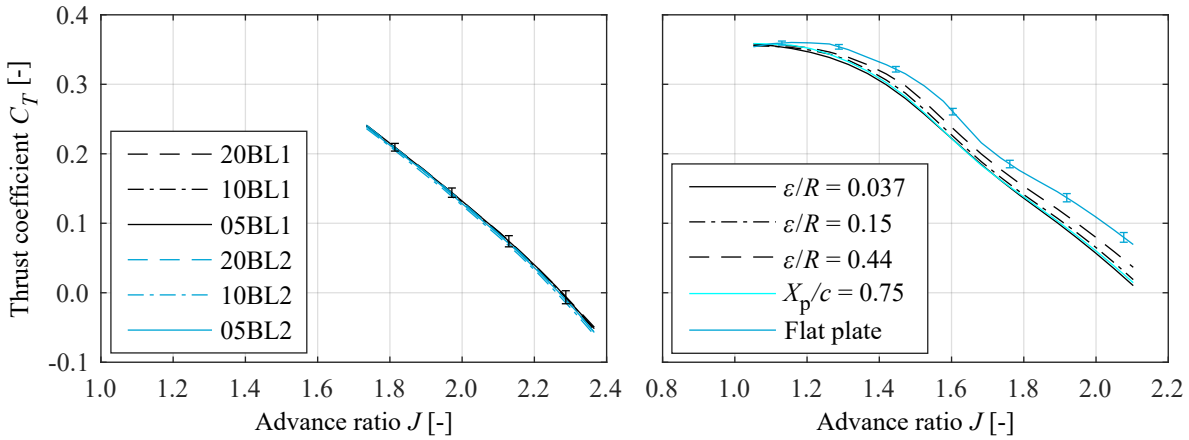

a) Effect of boundary-layer thickness (Flat plate, U_∞ = 40 m/s)

b) Effect of flap deflection and propeller position (BL1, U_∞ = 20 m/s)

Fig. 7 Propeller thrust curves, measured for different tip-clearances, boundary-layer thicknesses (left), and flap deflections and propeller positions (right). The measurements of sub-figure (b) correspond to $\delta_f = 20^o$, $X_p/c = 0.8$, $\varepsilon/R = 0.037$, unless otherwise specified by the legend.

[†]The equivalent turbulent flat-plate Reynolds number is defined as $Re_{FP} = (\rho_\infty U_\infty x_{FP})/\mu$, where μ is the dynamic viscosity and x_{FP} is the distance to the virtual origin of the equivalent flat plate, computed using $\delta_{99} = 0.37 x_{FP} (\rho_\infty U_\infty x_{FP}/\mu)^{-1/5}$ [29].

For the flapped configuration, on the other hand, a small increase in thrust is observed as the separation distance between the propeller and the wing is increased. This can be seen by comparing the black curves of Fig. 7b for a given advance ratio, and is attributed to a reduced inflow velocity at the propeller disk as the propeller is moved away from the wing surface. This shows that the inviscid effect of the wing on the propeller is dominant compared to the effect of the boundary layer, given that the impact of the boundary layer on propeller performance is even smaller in the flapped configuration than in the flat-plate configuration since $\delta_{99,\text{flapped}} < \delta_{99,\text{flat-plate}}$. Figure 7b also shows that placing the propeller at $X_p/c = 0.75$ instead of the baseline $X_p/c = 0.80$ has a negligible effect on propeller thrust. Finally, for the same advance ratio, the thrust produced in the flapped configuration is lower than in the flat-plate configuration, due to increased flow velocity surrounding the flap hinge.

IV. Time-Averaged Interaction Effects

The time-averaged aerodynamic interaction between the propeller and the wing boundary-layer is described in two steps. First, the impact on the wing pressure distributions is discussed in Sec. IV.A. These pressure distributions are then related to the ensemble-averaged flow field in Sec. IV.B.

A. Impact of Propeller on Surface Pressure Distributions

Figure 8 presents the pressure-coefficient distributions obtained directly below the propeller axis ($Z/R = 0$) for the flat-plate and flapped configurations. The pressure coefficient is presented as a difference with respect to propeller-off conditions, i.e. $\Delta C_p = C_{p,\text{on}} - C_{p,\text{off}}$. Figure 8a evidences the pressure decrease ahead of the propeller and pressure increase behind the propeller, as expected from earlier studies of propellers operating in close proximity to a flat wall [21] or above a wing profile [14]. From Fig. 8a it is evident that the propeller induces a favorable pressure gradient ($\mathrm{d}C_p/\mathrm{d}X < 0$) "far" upstream and downstream of the propeller disk, but a strong adverse pressure gradient in the vicinity of the propeller disk. The amplitude of the pressure peaks increases with increasing thrust coefficient, and is lower in the flat-plate configuration than in the flapped configuration (Fig. 8b). In the latter, the pronounced ΔC_p peak generated behind the propeller is caused directly by the increased static pressure behind the propeller disk on one hand, and indirectly by the reduction of the effective airfoil curvature due to propeller-induced flow separation on the other. This reduces the suction peak over the flap, effectively leading to an increase in ΔC_p. The propeller-induced flow separation also leads to negative ΔC_p values downstream of the propeller, which remain negative until the trailing edge of the airfoil (located at $X'/R = 2.2$). Finally, it is worth noting the secondary suction peak observed at $X'/R = 0.4$ for $C_T = 0.35$ in Fig. 8a and for $C_T = 0.1, 0.2$ in Fig. 8b. The peak was observed in repeated measurements and was also identified at a more downstream location for larger tip-clearances ($\varepsilon/R = 0.075$; not shown in this paper), suggesting that it is not a measurement error, but a local aerodynamic effect. This local effect may be triggered by surface imperfections, since it occurs immediately downstream of the flap hinge. However, an increased spatial resolution would be required to draw any conclusions in this regard.

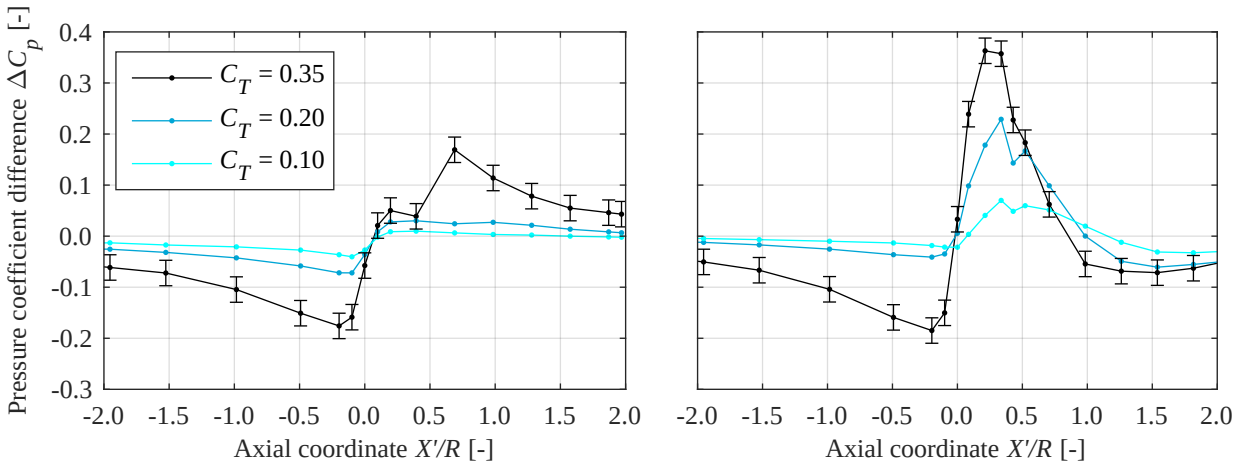

a) Flat plate configuration **b) Flapped configuration**

Fig. 8 Pressure coefficient distributions on the flat plate (left) and flapped (right) configurations for different propeller thrust settings (U_∞ = 20 m/s, ε/R = 0.037). Error-bars are only shown for C_T = 0.35 for clarity.

The adverse pressure gradient generated below the propeller disk plays an important role in boundary-layer separation. For this reason, Fig. 9 presents the pressure gradient recorded directly below the center of the propeller disk in the flat-plate configuration, for different boundary-layer thicknesses, tip clearances, and thrust settings. A non-dimensional pressure gradient is defined as the derivative of the pressure coefficient with respect to the axial coordinate (normalized with propeller radius). In order to remove the pressure gradients generated by the nacelle and surface imperfections (see Fig. 5), Fig. 9 presents the difference between the pressure gradient measured with the propeller on and the one measured with the propeller removed, which is equal to $\mathrm{d}(\Delta C_p)/\mathrm{d}(X/R)$. Note that the thrust coefficient T_c is plotted on the x-axis instead of C_T. Figure 9 shows a clear linear trend between the adverse pressure gradient on the wing surface and the propeller thrust coefficient. Another relevant observation in Fig. 9 is that the slope of the linear trends increases monotonically with increasing tip clearance ε/R. The impact of boundary-layer thickness has a negligible effect except at very low thrust coefficients, confirming that this interaction effect is predominantly of inviscid nature.

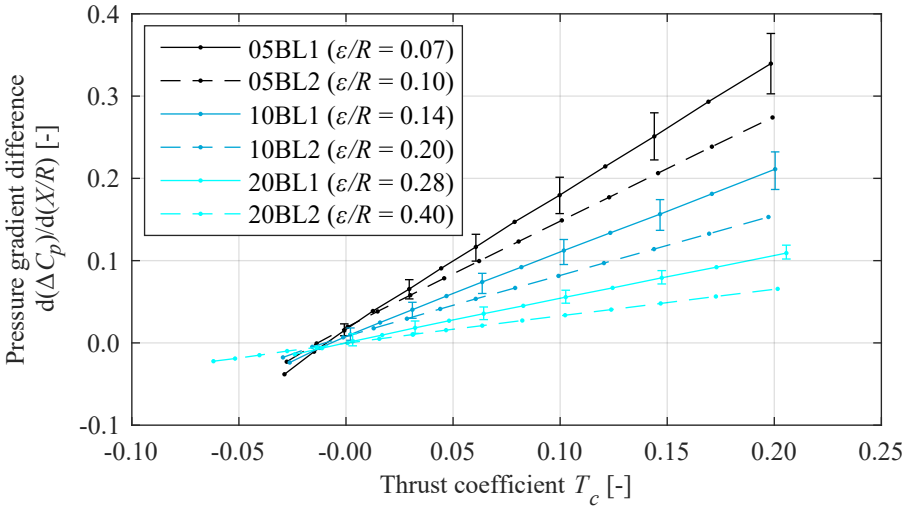

Fig. 9 Non-dimensional pressure-gradient generated by the propeller on the wing surface below the propeller disk in flat-plate configuration (U_∞ = 40 m/s). Error-bars are only plotted for curves corresponding to "BL1" for clarity.

B. Time-Averaged Flow Phenomena

In order to analyze how the changes in surface pressure relate to the flow field, Fig. 10 presents the axial velocity field obtained in the vicinity of the propeller. The velocity fields include data from both the small and the large FOVs. For reference, Figs. 10a and 10b present the velocity contours in propeller-off conditions. In the flat-plate configuration (Fig. 10a), a small increase in axial velocity is caused by the blockage of the nacelle. In the flapped configuration (Fig. 10b), the curvature at the flap hinge accelerates the flow further. This leads to a thinner boundary layer over the flap hinge, although it rapidly grows downstream. Figures 10c and 10d show the same fields, but with the propeller at a high thrust setting. These plots include velocity vectors which represent the difference between propeller-on and propeller-off conditions, $[\Delta U, \Delta V] = [(U_{\mathrm{on}} - U_{\mathrm{off}}), (V_{\mathrm{on}} - V_{\mathrm{off}})]$. In other words, they represent the in-plane velocities which are, directly or indirectly, induced by the propeller.

The increased velocity in the propeller slipstream is evident in Figs. 10c and 10d. The increase is largest at the outboard portion of the blade, since the maximum blade loading occurs at approximately 80% of the blade radius [28]. For the flat plate configuration (Fig. 10c), the slipstream exhibits a strong contraction at the location of the propeller disk. From $X'/R = 0.4$ to $X'/R = 0.8$, the velocities present a negative V component, and the slipstream gradually approaches the wall. Consequently, immediately downstream of the propeller, a region of reduced velocity is generated near the wall which extends until approximately $X'/R = 0.5$. Although the axial velocity is significantly reduced in this region ($\Delta U < 0$), it should be noted that the velocity is still positive, and the flow does not separate. Downstream of this region, the gradual displacement of the slipstream towards the surface leads to a substantial reduction in boundary layer thickness; in fact, the reduction is such that the boundary layer is no longer visible in the FOV. This downwards displacement of the slipstream is attributed to the spanwise pressure distribution generated by the propeller. Previous studies [14] have shown that the pressure peaks observed in Fig. 8 are maximum below the propeller axis ($Z/R = 0$),

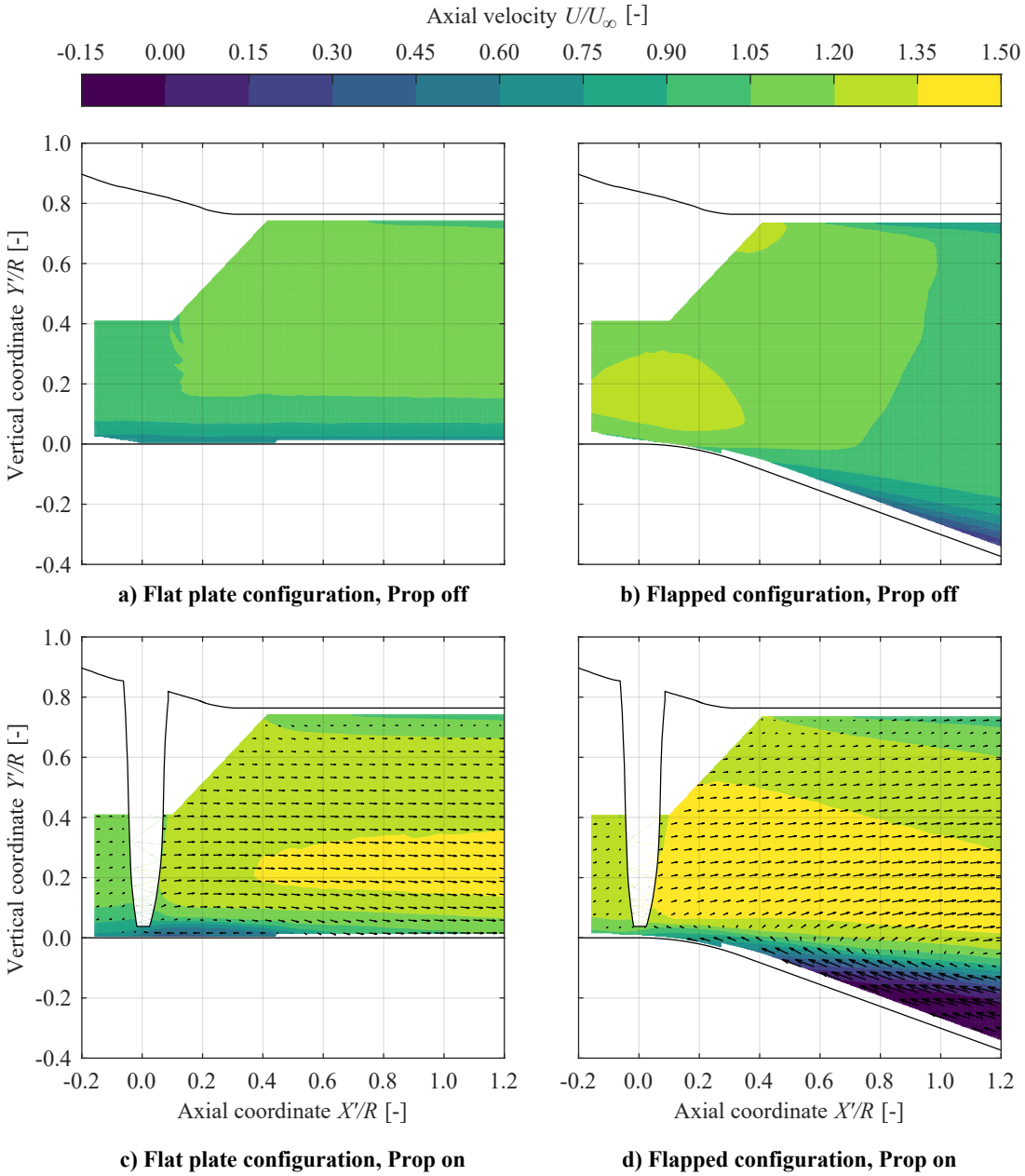

Fig. 10 Time-averaged axial velocity contours of the flat plate (left) and flapped (right) configurations, with the propeller off (top) and on (bottom). The velocity vectors represent the in-plane velocity components induced by the propeller (U_∞ = 20 m/s, ε/R = 0.037, C_T = 0.35).

and thus, near the wall, the spanwise pressure gradient forces the flow to move away from $Z/R = 0$. This would leave a mass deficit at the centerline and, consequently, the flow in the propeller slipstream must approach the wall to maintain continuity. However, additional data regarding the spanwise velocity distribution outside the $Z/R = 0$ plane would be required to verify this hypothesis.

When an additional pressure gradient is generated by deflecting the flap (Fig. 10d), the flow separates immediately downstream of the propeller, and a region of reverse flow ($U < 0$) is generated over the flap. Several factors contribute towards flow separation. Firstly, since the propeller significantly increases the axial momentum of the flow, a large change in vertical momentum is needed in order to deflect the slipstream along the flap surface. This would require a strong suction force over the flap hinge which the boundary layer is unable to withstand, partially due to the propeller-induced adverse pressure gradient discussed in the previous section. The adverse pressure gradient is generated not only due to

the static pressure jump created across the propeller disk, but also due to the contraction of the slipstream, as evidenced in Fig. 10c. Moreover, the rotation of the propeller blades leads to pressure perturbations in the boundary layer which increase its tendency to separate from the surface. This unsteady effect is described in the following section.

V. Unsteady Interaction Effects

This section discusses the unsteady component of the interaction that takes place between the propeller and the wing boundary-layer. To this end, Sec. V.A describes the unsteady phenomena present in the flow field, while Sec. V.B discusses the pressure fluctuations perceived on the wing surface due to these phenomena.

A. Time-Dependent Flow Phenomena

Figure 11 presents the phase-averaged flow field downstream of the propeller for the flat-plate and flapped configurations. In this case, contours of normalized out-of-plane vorticity[‡] are shown, in order to clearly identify the flow structures. The velocity vectors again represent the velocities induced by the propeller, that is, the difference between the phase-averaged velocity distributions and the ones of Fig. 10a and 10b. In both cases, the phase angle of the propeller is such that one blade has just exited the measurement plane, and the associated blade wake and tip vortex (labeled as the "1st vortex" in Fig. 11a) are visible at the upstream end of the FOV. The negative vorticity trailing from the outboard segment of the blade is clearly visible in these blade wakes, while in the wake of the previous blade, most negative vorticity has rolled up into a strong tip vortex (2nd vortex). The positive vorticity regions near the nacelle surface are a combination of the root vortices and the shear in the nacelle's boundary layer. For the flapped configuration, a region of increased (negative) vorticity can be seen detached from the flap surface. This region corresponds to the shear layer between the slipstream and the region of reverse flow over the flap. The velocities induced by the tip vortices are also clearly visible. In the flat-plate configuration, these induced velocities generate a local axial velocity deficit between the wall surface and the vortex core. Since these vortices are convected downstream, on average the low-velocity region of Fig. 10c is generated. Analysis of additional phase-free datasets confirmed that, although negative axial velocities existed in the vicinity of the vortex core, no local flow reversal occurred at the wall.

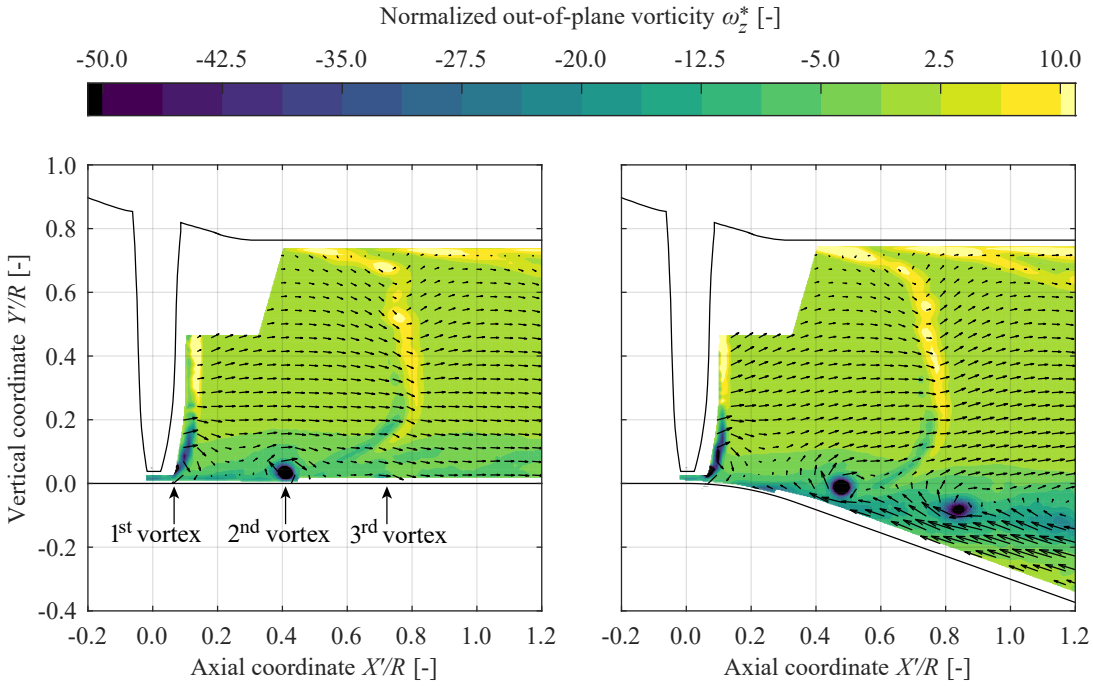

a) Flat plate configuration **b) Flapped configuration**

Fig. 11 Phase-averaged vorticity contours of the flat plate (left) and flapped (right) configurations. The velocity vectors represent the in-plane velocity components induced by the propeller (U_∞ = 20 m/s, ε/R = 0.037, C_T = 0.35). The color map does not span the full range of ω_z^* values.

[‡]Vorticity is normalized using the propeller diameter and the velocity at the propeller disk, estimated using actuator disk theory: $\omega_z^* = \omega_z D_p / U_{AD}$.

In Fig. 11a, a third vortex is located at $X'/R = 0.7$ near the bottom edge of the FOV. The associated blade wake is downstream of the FOV, since the wake is rapidly convected at the slipstream velocity, while the tip vortex is convected slowly inside the boundary layer (the same occurs in Fig. 11b). An evaluation of the individual PIV images indicated two reasons why this vortex does not appear prominently in the vorticity field. Firstly, while the tip vortices are periodic in nature, the eddies in the turbulent boundary layer are not. Hence, for each phase-locked image, the tip vortices are at a slightly different location, due to the randomness of the velocity fluctuations which convect the vortices. The extent of this tip-vortex meandering increases as the tip vortices are convected downstream. Consequently, when computing the phase-averaged flow field, the vortex core is smeared out, and less concentrated than in an instantaneous velocity field. For this same reason, the vortex located at $X'/R = 1.1$ in the flapped configuration (Fig. 11b) apparently presents a low vorticity magnitude. In this configuration, the position of the shear layer which separates the slipstream from the recirculating region varies over time, since the flow is excited by periodic tip vortices on one hand, and by random structures in the boundary layer on the other. As a consequence, the position of the tip vortex differs appreciably from one blade passage to another. A second reason why the tip vortex at $X'/R = 0.7$ is not clearly visible in Fig. 11a, is the increased viscous dissipation that takes place when the vortex core approaches the wall, due to the downwards displacement of the slipstream edge discussed in Fig. 10c. Individual PIV images showed that, in this region, the vorticity magnitude in the vortex core had diminished or—in some cases—that the vortex core had disappeared completely.

In order to confirm that the vortex dissipation is not an artifact of a limited spatial resolution, Fig. 12 presents a close-up of the interaction surrounding one of the tip vortices. This figure presents a different phase angle than Fig. 11, such that the tip vortex is located in the small FOV. Figure 12 presents contours of the out-of-plane (spanwise) velocity component in order to highlight the flow features, together with velocity vectors of the propeller-induced in-plane velocities. The blade wake, which represents a velocity deficit in the blade frame-of-reference, appears as a strong swirl velocity in the inertial reference frame. Furthermore, large positive and negative values of the spanwise velocity are induced on either side of the vortex core, since the vortex filament is oblique to the sampling plane.

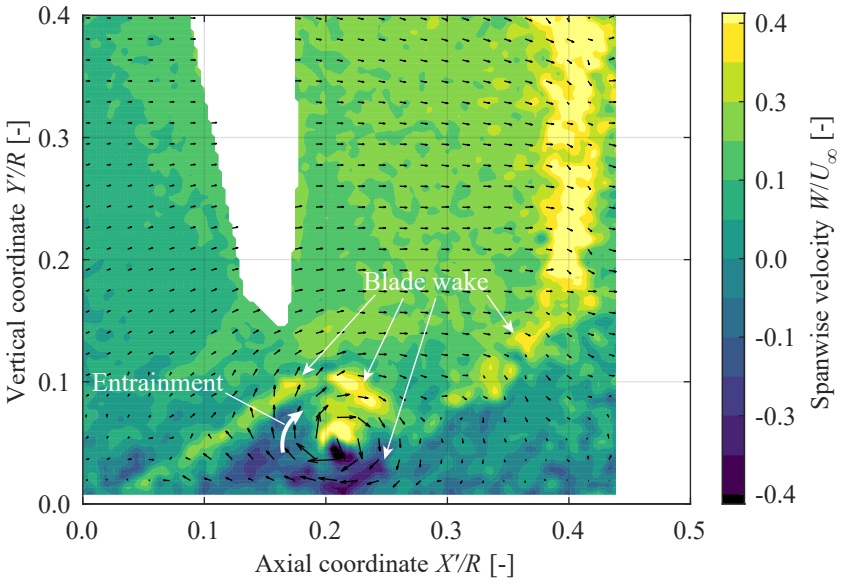

Fig. 12 Close-up view of an instantaneous out-of-plane velocity field in the flat-plate configuration. The velocity vectors represent the in-plane velocity components induced by the propeller ($U_\infty = 20$ m/s, $\varepsilon/R = 0.037$, $C_T = 0.35$). The blank region of the FOV is blocked by a blade outside the measurement plane. The color map does not span the full range of W/U_∞ values.

The most notable flow feature in Fig. 12 is the sheet of increased and decreased spanwise velocity that appear to roll up above and below the vortex core, respectively. This structure is not visible in phase-averaged flow fields, since in each blade passage it varies in position and strength—occasionally not appearing at all—as a consequence of the random interaction with the eddies in the turbulent boundary-layer. When comparing this velocity distribution to typical velocity distributions in an isolated-propeller slipstream [30], it becomes evident that these sheets constitute the outer

portion of the blade wakes, which in undisturbed conditions roll up into the tip vortex. However, due to the presence of the wall boundary layer, the lower segments of the blade wake start lagging behind, and a discontinuity is formed. Furthermore, the swirl induced by the vortex entrains low-momentum fluid from the bottom of the boundary layer, causing it to move away from the wall and wrap around the vortex. This locally increases the dissipation rate of the tip vortex, eventually causing it to disappear, as discussed in Sec. V.B. The gradual decrease in vortex strength also implies that, for a given vortex, the velocities induced by the succeeding (upstream) vortex are higher in magnitude than the velocities induced by the preceding (downstream) one. This leads to a net downwards-oriented induced velocity on the vortex filament, which may contribute to the downwards displacement of the slipstream discussed in Fig. 11c.

It is worth highlighting that the flow phenomena described so far are originated in the trailing vortex system of the propeller. The highly unsteady formation of secondary vortical structures and areas of reverse flow observed below the propeller disk in the work of Murray et al. [21] were not encountered in this experiment. Although this may be due to a limited spatial or temporal resolution, it is most likely because the experiment of Murray et al. presented a thicker boundary layer ($\delta_{99}/R \approx 0.44$), and the propeller tip was positioned deeper inside the boundary layer. In other words, in this experiment, the local advance ratio of the blade tip is not low enough to trigger ground-vortex effects. This is consistent with the predictions of Sato et al. [24], who developed a relation between the thrust coefficient, tip clearance, and the type of flow instabilities that occur below the propeller disk. Although their experiments were performed at higher thrust coefficients, the model suggests that no vortices or reverse flow are produced for the combination of thrust coefficients and tip-clearance in this experiment.

B. Propeller-Induced Surface Pressure Fluctuations

The unsteady flow features identified in the previous section lead to pressure fluctuations on the wing surface. In order to visualize the distribution of these pressure fluctuations, Fig. 13 presents contours of the root-mean-square (rms) of the unsteady pressure coefficient, measured across the wing surface using the embedded microphones. The unsteady pressure coefficient is obtained by normalizing the measured pressure fluctuations with freestream dynamic pressure, i.e. $C'_p = p'/(0.5\rho_\infty U_\infty^2)$. However, analysis of the raw microphone data showed that, in the vicinity of the propeller disk, the maximum input level of the microphones was exceeded at several locations. The locations are indicated by white crosses in Fig. 13. This led to cropped microphone signals, and therefore the magnitudes at these locations are incorrect (conservative). Nevertheless, several important conclusions can be drawn by analyzing the distributions.

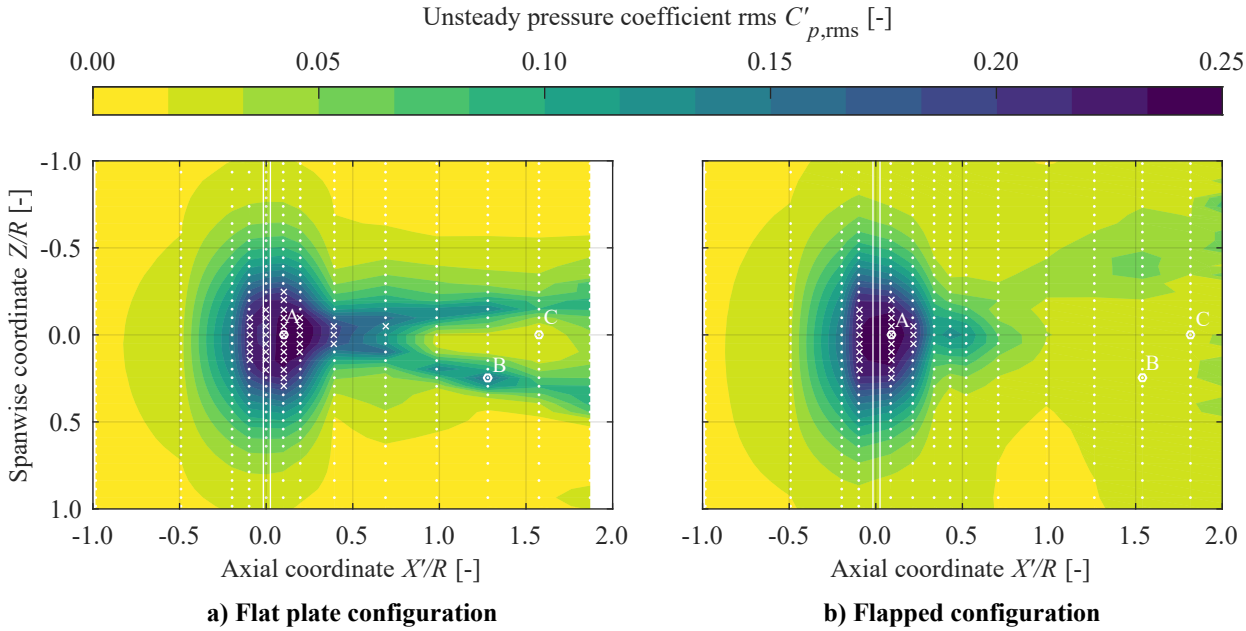

Fig. 13 Unsteady pressure coefficient contours on the wing surface. The white lines indicate the axial position of the leading edge and trailing edge of the blade tip, respectively. Dots indicate measurement locations, while crosses indicate locations where the maximum input level of the microphone was exceeded. The circular markers indicate the locations sampled in Fig. 14 (U_∞ = 20 m/s, ε/R = 0.037, C_T = 0.35).

Firstly, Fig. 13 evidences that the pressure fluctuations on the wing surface are not negligible, given that their amplitude exceeds the time-averaged effect of the propeller on the surface pressure distributions (see Fig. 8). Secondly, two distinct regions of pressure fluctuations can be identified. The first corresponds to the oval-like region below the propeller disk, which is generated by the pressure field induced by the propeller blades. As the blades rotate, an observer on the wing surface perceives periodic variations in static pressure. The second region is generated by the vortical structures in the propeller slipstream, which increase the pressure fluctuations downstream of the propeller ($X'/R > 0$). Based on the distance between the vortex cores and the wing surface observed in Figs. 11 and 12, these fluctuations are caused by the velocities induced by the tip vortices near the wall, and not by the low static pressure created inside the vortex core. Hence, there are two main sources of pressure perturbations: the static pressure fluctuations induced directly by the propeller blades, and the velocity fluctuations induced by the tip vortices. Of the two sources, the first one is dominant. Due to the superposition of the two, the highest pressure fluctuations are recorded slightly downstream of the propeller disk in the flat-plate configuration, rather than directly beneath it. For the flapped configuration, the fluctuations generated by the propeller slipstream are lower than for the flat-plate configuration, because the slipstream has separated from the flap surface. Thus, the velocity fluctuations induced by the trailing vortex system on the flap surface are reduced. Consequently, Fig. 13b shows a wide region of modest pressure fluctuations, generated by the turbulent flow in the separated region behind the propeller. These pressure fluctuations are higher on the down-going blade side ($Z/R < 0$) than on the up-going blade side ($Z/R > 0$), indicating an asymmetry in the flow field. Additional flow-field visualization outside the $Z/R = 0$ plane is required to determine the cause of this asymmetry.

The most counterintuitive observation in Fig. 13 is that, in the flat-plate configuration, the high-$C'_{p,\mathrm{rms}}$ region beneath the slipstream splits into two branches downstream. This is suggests that the viscous interaction between the tip vortices and the boundary layer fully dissipates the vortical structures, thus removing the periodic perturbations along the centerline of the wing. The two branches of high $C'_{p,\mathrm{rms}}$-values correspond to the edges of the slipstream, where the previously helicoidal vortex filaments are now severed and locally oblique to the wing surface. In order to confirm that the reduction is indeed caused by a decrease in periodic perturbations, and not by a reduction in broadband noise levels, Fig. 14 gathers the pressure spectra sampled at the three locations marked by the white circles in Fig. 13. The reader is reminded that, at location A, the maximum excitation amplitude of the microphones was exceeded. Therefore, the non-monotonic evolution of the tonal peaks, as well as the secondary peaks observed between consecutive blade-passage frequency (BPF) multiples, are most likely an artifact of the cropped pressure waveforms registered by the microphones. Nevertheless, the spectra confirm that the tonal components at integer multiples of the blade passage frequency are the dominant source of pressure fluctuations.

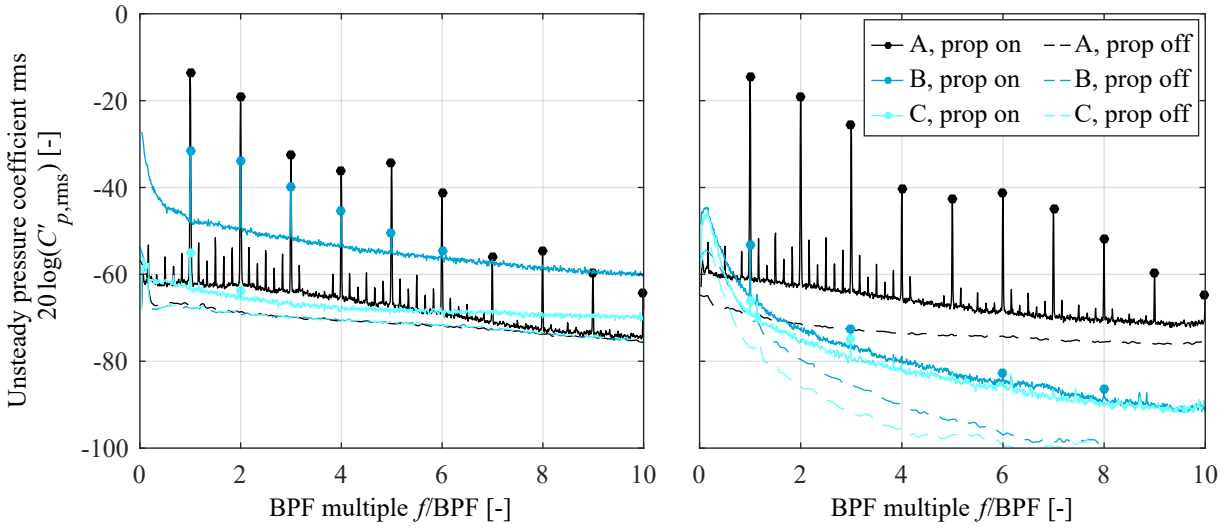

a) Flat plate configuration (BPF = 482 Hz) **b) Flapped configuration (BPF = 531 Hz)**

Fig. 14 Spectra of the pressure fluctuations observed on the wing surface at the locations indicated in Fig. 13 (U_∞ = 20 m/s, ε/R = 0.037, C_T = 0.35). Note that the maximum excitation amplitude of the microphone was exceeded at location A in the propeller-on case.

When comparing the spectra of Fig. 14a at locations A and C, it becomes evident that the tonal components have indeed disappeared in the latter. However, even though the broadband component of the two spectra are comparable, the downstream one (location C) presents slightly lower broadband levels up to $f \approx 5$BPF (2500 Hz). This indicates a reduction of the large-scale fluctuations inside the turbulent boundary layer. In any case, the broadband levels are higher than in propeller-off conditions. By comparing the spectra of Fig. 14a at locations A and B, on the other hand, one can see that the tonal peaks are higher for the former, while the broadband levels are lower. This confirms that the main contributor to the pressure fluctuations at location A are the fluctuations generated by the passing blades, which are not present at the downstream location. At the downstream location, however, the increase in broadband levels indicates that the interaction between the tip vortices and the boundary layer have increased the turbulent fluctuations in the boundary-layer. Finally, Fig. 14b shows that the tonal pressure fluctuations disappear downstream due to the detachment of the slipstream from the flap surface. However, the increase in broadband levels with respect to propeller-off conditions shows that additional perturbations are induced in the separated-flow region due to the propeller slipstream.

VI. Effect of Propeller Position and Thrust Setting on Flow Separation

Now that the aerodynamic phenomena that affect flow separation have been presented, it is relevant to analyze how flow separation is affected by different operating conditions and design parameters. To this end, Fig. 15 presents the phase-averaged flow fields downstream of the propeller for different thrust settings, tip-clearances, and axial positions of the propeller. Figure 15a is in essence the same as Fig. 11b, but has been included here without the small FOV for comparison with the other plots.

The effect of propeller thrust can be observed by comparing Figs. 15a, 15c, and 15e. At lower thrust coefficients, the flow separation is less severe. This is, however, not a solution from a design perspective, since $C_T < 0.2$ is representative of cruise conditions, but not of low-speed conditions. At $C_T = 0.1$ (Fig. 15e), the slipstream velocities induced by the propeller in the PIV plane are negligible, even though the thrust coefficient is positive. This is a consequence of the accelerated flow over the flap hinge, which locally increases the effective advance ratio, reducing the thrust to practically zero while the top half of the propeller disk still generates thrust. Nevertheless, the bottom-right corner of Fig. 15e shows that the propeller still generates an axial velocity reduction over the flap, leading to an earlier separation than in propeller-off conditions. This confirms that the unsteady excitation caused by the propeller blades is still detrimental for the boundary layer, even when the propeller generates practically no thrust.

The effect of the propeller's axial position can be analyzed by comparing Figs. 15a and 15b. When the propeller is moved half a radius ($0.05c$) upstream (Fig. 15b), the flow remains attached to the surface, and the slipstream deflects downwards. This is beneficial from a design perspective, because not only is the stall angle of the flap delayed, but also the effective lift is increased due to the deflection of the slipstream. This Coanda effect does not appear for the baseline $X_p/c = 0.8$, and can most easily be understood by referring to Fig. 10c. When the propeller is placed above the flap hinge ($X_p/c = 0.8$), the contraction of the slipstream generates a strong adverse pressure gradient and a tendency of the flow to separate from the surface. In this case, the resistance of the boundary-layer to flow separation is further decreased due to the strong pressure fluctuations generated by the propeller blades. Hence, when the additional pressure gradient is imposed by deflecting the flap, the flow separates. However, when the propeller is moved upstream ($X_p/c = 0.75$), the location of the flap hinge is approximately $0.5R$ downstream of the propeller, where the propeller slipstream attaches to the wall in flat-plate conditions. This leads to a thinner boundary layer which is more capable of resisting the adverse pressure gradient over the flap hinge. Moreover, the increased viscous interaction between the tip vortices and boundary layer weakens the periodic perturbations. A combination of these factors allows the flow to remain attached to the surface longer than in propeller-off conditions.

Finally, the effect of tip clearance is assessed by comparing Figs. 15a, 15d, and 15f. In Figs. 15d and 15f, the propeller operates outside the edge of the boundary layer. Even though the magnitude of the flow reversal decreases with increasing clearance, the flow over the flap remains detached even for the largest clearance (Fig. 15f). In this case, a channel of relatively undisturbed flow exists between the slipstream edge and the boundary layer, and the pressure fluctuations on the wing surface have been significantly reduced. However, the high-momentum slipstream acts as a boundary condition for the air beneath it, creating a divergent channel which increases the adverse pressure gradient with respect to propeller-off conditions, and causes the flow to separate. Thus, while in Fig. 15e the unsteady effects lead to flow separation, in Fig. 15f the time-averaged, inviscid effect of the propeller causes flow separation. This proves that both the steady and unsteady interaction effects can cause flow separation, and that the relative importance of the two contributions depends on the operating conditions and design of the system. In any case, Fig. 15f shows that increasing the tip-clearance, within the practical limits of over-the-wing propellers, is not an effective measure to delay flow separation.

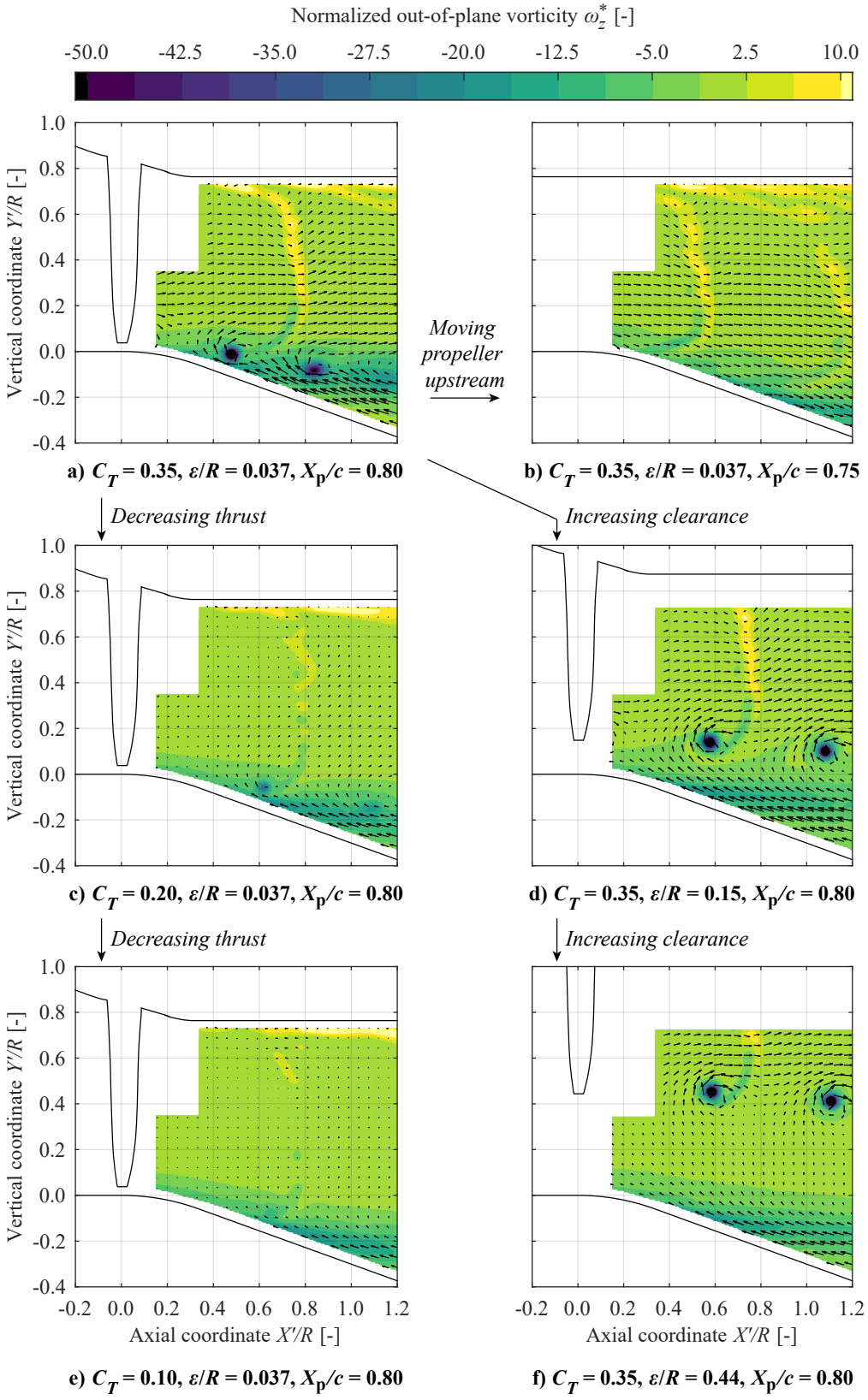

Fig. 15 Phase-averaged vorticity contours of the flapped configuration for different thrust settings, tip-clearances and axial positions of the propeller. The velocity vectors represent the in-plane velocity components induced by the propeller (U_∞ = 20 m/s). The color map does not span the full range of ω_z^* values.

VII. Conclusions & Recommendations

A wind-tunnel experiment has been carried out with the objective of studying the aerodynamic interaction between an over-the-wing (OTW) propeller and the wing boundary-layer. This interaction affects the separation of the boundary layer, and therefore has an important impact on the maximum lift coefficient attainable with OTW systems. In order to understand the underlying flow phenomena, first the time-averaged impact of a propeller placed in close proximity to a flat plate is analyzed. Results show that an adverse pressure gradient is generated below the propeller disk which increases linearly with thrust, and decreases with increasing tip clearance. The contraction of the slipstream, which is partially responsible for this adverse pressure gradient, generates a region of reduced axial velocity between the slipstream edge and the wall surface. This region of reduced velocity extends up to approximately $0.5R$ downstream of the propeller disk, beyond which the slipstream adheres to the wall and the thickness of the boundary layer is significantly reduced. In this process, the propeller tip-vortices are forced towards the wall, where they are eventually dissipated due to viscous interaction with the boundary layer. Consequently, the pressure perturbations produced by the slipstream on the surface below the propeller axis decrease in axial direction. However, the dominant source of pressure fluctuations are the static pressure fields created by the passing blades. Together, these two sources lead to pressure fluctuations whose amplitude exceeds the magnitude of the time-averaged changes in pressure on the surface.

When the propeller is positioned above the hinge line and an additional adverse pressure gradient is imposed by deflecting the flap, the aforementioned effects lead to flow separation over the flap. The magnitude of the flow reversal increases with increasing thrust coefficient. Increasing the clearance between the propeller and the wing surface is an ineffective approach to mitigate this problem, since flow separation is observed even when the tip-clearance is at least three times the boundary-layer thickness. However, placing the propeller half a radius upstream is an effective measure to avoid flow separation. In that case, the low-velocity region generated by the slipstream contraction, as well as the high-amplitude pressure perturbations, are located upstream of the flap hinge. At the flap hinge, the slipstream has adhered to the wall, leading to a thinner boundary-layer which is more capable of withstanding the adverse pressure gradient over the flap. This leads to a Coanda effect which deflects the slipstream downwards and improves the flap performance with respect to propeller-off conditions.

However, earlier studies show that placing the propeller further upstream is detrimental for propeller efficiency in cruise conditions. Therefore, deflecting the propeller with the flap constitutes a promising alternative to mitigate the flow separation over the flap. This would, additionally, lead to an effective lift increase due to thrust vectoring, and is therefore left for future research. Furthermore, the impact of multiple propellers on the flow separation and Coanda effect should be assessed. Finally, an increased dynamic range and spatial resolution of the microphones would provide the instantaneous pressure distributions and gradients across the wing surface. Such data would provide additional knowledge on the relative importance of the steady and unsteady interaction effects, and how these can be mitigated. A deeper understanding of these phenomena will enable a more effective design of over-the-wing distributed-propulsion systems.

Acknowledgments

This research is part of the European Union's Horizon 2020 Clean Sky 2 Large Passenger Aircraft program (CS2-LPA-GAM-2014-2015-01). The authors would like to thank Tomas Sinnige, Biagio Della Corte, and Stefan Bernardy for their help with the wind-tunnel experiments. The authors would also like to thank Jan Lisberg Jacobsen and Elrick L. Cornelius for providing the Sonion microphones.

References

[1] Bonet, J. T., Schellenger, H. G., Rawdon, B. K., Elmer, K. R., Wakayama, S. R., Brown, D. L., and Guo, Y., "Environmentally Responsible Aviation (ERA) Project - N+2 Advanced Vehicle Concepts Study and Conceptual Design of Subscale Test Vehicle (STV): Final Report," Technical Report NASA/CR-2011-216519, December 2011.

[2] Advisory Council for Aviation Research and Innovation in Europe (ACARE), "Realising Europe's vision for aviation: Strategic research & innovation agenda, Vol. 1," Advisory Council for Aviation Research and Innovation in Europe, 2012.

[3] Felder, J. L., Brown, G. V., Kim, H. D., and Chu, J., "Turboelectric Distributed Propulsion in a Hybrid Wing Body Aircraft," 20th International Society for Airbreathing Engines (ISABE) Conference, Gothenburg, Sweden, September 12-16 2011.

[4] Isikveren, A. T., Seitz, A., Bijewitz, J., Mirzoyan, A., Isyanov, A., Grenon, R., Atinault, O., Godard, J. L., and Stückl, S., "Distributed propulsion and ultra-high by-pass rotor study at aircraft level," *The Aeronautical Journal*, Vol. 119(1221), 2015, pp. 1327–1376.

[5] Voskuijl, M., van Bogaert, J., and Rao, A. G., "Analysis and design of hybrid electric regional turboprop aircraft," *CEAS Aeronautical Journal*, Vol. 9, 2018, pp. 15–25.

[6] Kim, H. D., "Distributed Propulsion Vehicles," 27th Congress of the International Council of the Aeronautical Sciences, Nice, France, September 19-24 2010.

[7] Borer, N. K., Patterson, M. D., Viken, J. K., Moore, M. D., Clarke, S., Redifer, M. E., Christie, R. J., Stoll, A. M., Dubois, A., Bevirt, J. B., Gibson, A. R., Foster, T. J., and Osterkamp, P. G., "Design and Performance of the NASA SCEPTOR Distributed Electric Propulsion Flight Demonstrator," 16th AIAA Aviation Technology, Integration, and Operations Conference, Washington, DC, USA, June 13-17 2016.

[8] Müller, L., Heinze, W., Kožulović, D., Hepperle, M., and Radespiel, R., "Aerodynamic Installation Effects of an Over-the-Wing Propeller on a High-Lift Configuration," *Journal of Aircraft*, Vol. 51(1), 2014, pp. 249–258.

[9] Johnson Jr., J. L., and White, E. R., "Exploratory Low-Speed Wind-Tunnel Investigation of Advanced Commuter Configurations Including an Over-the-Wing Propeller," AIAA Aircraft Design, Systems and Technology Meeting, Fort Worth, TX, USA, October 17-19 1983.

[10] Broadbent, E. G., "Noise shielding for aircraft," *Progress In Aerospace Sciences*, Vol. 17, 1977, pp. 231–268.

[11] Beck, S. C., Müller, L., and Langer, S. C., "Numerical assessment of the vibration control effects of porous liners on an over-the-wing propeller configuration," *CEAS Aeronautical Journal*, Vol. 7(2), 2016, pp. 275–286.

[12] Veldhuis, L. L. M., "Propeller Wing Aerodynamic Interference," PhD Dissertation, Delft University of Technology, 2005.

[13] de Vries, R., Hoogreef, M. F. M., and Vos, R., "Preliminary Sizing of a Hybrid-Electric Passenger Aircraft Featuring Over-the-Wing Distributed-Propulsion," 2019 AIAA Aerospace Sciences Meeting, San Diego, CA, USA, January 7-11 2019.

[14] Marcus, E. A. P., de Vries, R., Raju Kulkarni, A., and Veldhuis, L. L. M., "Aerodynamic Investigation of an Over-the-Wing Propeller for Distributed Propulsion," 2018 AIAA Aerospace Sciences Meeting, Kissimmee, FL, USA, January 8-12 2018.

[15] Müller, L., Kožulović, D., and Radespiel, R., "Aerodynamic performance of an over-the-wing propeller configuration at increasing Mach number," *CEAS Aeronautical Journal*, Vol. 5, 2014, pp. 305–317.

[16] Müller, L., Friedrichs, J., and Kožulović, D., "Unsteady Flow Simulations of an Over-the-wing Propeller Configuration," 50th AIAA/ASME/SAE/ASEE Joint Propulsion Conference, Cleveland, OH, USA, July 28-30 2014.

[17] Peridier, V. J., Smith, F. T., and Walker, J. D. A., "Vortex-induced boundary-layer separation. Part 2. Unsteady interacting boundary-layer theory," *Journal of Fluid Mechanics*, Vol. 232, 1991, pp. 133–165.

[18] Sengupta, T. K., and Sarkar, S., "Vortex-induced instability of an incompressible wall-bounded shear layer," *Journal of Fluid Mechanics*, Vol. 493, 2003, pp. 277–286.

[19] Doligalski, T. L., Smith, C. R., and Walker, J. D. A., "Vortex interactions with walls," *Annual Review of Fluid Mechanics*, Vol. 26(1), 1994, pp. 573–616.

[20] Straus, J., and Mayle, R. E., "Boundary-layer measurements during a parallel blade-vortex interaction," 10th Applied Aerodynamics Conference, Palo Alto, CA, USA, June 22-24 1992.

[21] Murray IV, H. H., Devenport, W. J., Alexander, W. N., Glegg, S. A. L., and Wisda, D., "Aeroacoustics of a rotor ingesting a planar boundary layer at high thrust," *Journal of Fluid Mechanics*, Vol. 850, 2018, pp. 212–245.

[22] Yang, Y., Sciacchitano, A., Veldhuis, L. L. M., and Eitelberg, G., "Analysis of propeller-induced ground vortices by particle image velocimetry," *Journal of Visualization*, Vol. 21(1), 2018, pp. 39–55.

[23] Martio, J., Sipilä, T., Sanchez-Caja, A., Saisto, I., and Siikonen, T., "Evaluation of the Propeller Hull Vortex Using a RANS Solver," Second International Symposium on Marine Propulsors, Hamburg, Germany, June 15-17 2011.

[24] Sato, R., Tasaki, R., and Nishiyama, S., "Observation of flow on a horizontal flat plate above a working propeller and physics of propeller-hull vortex cavitiation," Proceedings of the International Symposium on Propeller and Cavitation, Wuxi, China, April 8-12 1986.

[25] Lin, N., Reed, H. L., and Saric, W. S., "Effect of leading-edge geometry on boundary-layer receptivity to freestream sound," *Instability, Transition, and Turbulence*, Springer, New York, NY, 1992, pp. 421–440.

[26] Li, Q., Öztürk, K., Sinnige, T., Ragni, D., Eitelberg, G., Veldhuis, L. L. M., and Wang, Y., "Design and Experimental Validation of Swirl-Recovery Vanes for Propeller Propulsion Systems," *AIAA Journal*, Vol. 56(12), 2018, pp. 4719–4729.

[27] Ewald, B. F. R., *Wind Tunnel Wall Corrections (la Correction des effets de paroi en soufflerie)*, Advisory Group for Aerospace Research and Development (AGARD-AG-336), 1998.

[28] van Arnhem, N., Vos, R., and Veldhuis, L. L. M., "Aerodynamic Loads on an Aft-Mounted Propeller Induced by the Wing Wake," 2019 AIAA Aerospace Sciences Meeting, San Diego, CA, USA, January 7-11 2019.

[29] Schlichting, H., *Boundary-Layer Theory*, 7th ed., New York: McGraw-Hill, 1979.

[30] Sinnige, T., de Vries, R., Della Corte, B., Avallone, F., Ragni, D., Eitelberg, G., and Veldhuis, L. L. M., "Unsteady Pylon Loading Caused by Propeller-Slipstream Impingement for Tip-Mounted Propellers," *Journal of Aircraft*, Vol. 55(4), 2018, pp. 1605–1618.